


# Understanding thermal hysteresis of ferroelectric phase transitions in $BaTiO_3$ with combined first-principle-based approach and phase-field model

Cancan Shao(邵灿灿) and Houbing Huang(黄厚兵)

**Citation:**Chin. Phys. B, 2025, 34 (**2**): 027701. DOI: 10.1088/1674-1056/ad9e94
Journal homepage: http://cpb.iphy.ac.cn; http://iopscience.iop.org/cpb

**What follows is a list of articles you may be interested in**

---

## Optimization of Skanavi model and its application to high permittivity materials

Hao Luo(罗昊), Xinrui Qin(秦新瑞), Kejia Geng(耿可佳), Cuncun Kong(孔存存), and Pengfei Cheng(成鹏飞)
Chin. Phys. B, 2025, 34 (**1**): 017702. DOI: 10.1088/1674-1056/ad9ba0

## Effects of Ni substitution on multiferroic properties in $Bi_5FeTi_3O_{15}$ ceramics

Hui Sun(孙慧), Jiaying Niu(钮佳颖), Haiying Cheng(成海英), Yuxi Lu(卢玉溪), Zirou Xu(徐紫柔), Lei Zhang(张磊), and Xiaobing Chen(陈小兵)
Chin. Phys. B, 2021, 30 (**10**): 107701. DOI: 10.1088/1674-1056/ac1b92

## Structure instability-induced high dielectric properties in[001]-oriented $0.68Pb(Mg_{1/3}Nb_{2/3})O_3$-$0.33PbTiO_3$ crystals

Xiao-Juan Li(李晓娟), Xing Fan(樊星), Zeng-Zhe Xi(惠增哲), Peng Liu(刘鹏), Wei Long(龙伟), Pin-Yang Fang(方频阳), Rui-Hua Nan(南瑞华)
Chin. Phys. B, 2019, 28 (**5**): 057701. DOI: 10.1088/1674-1056/28/5/057701

## Epitaxially strained $SnTiO_3$ at finite temperatures

Dawei Wang(王大威), Laijun Liu(刘来君), Jia Liu(刘佳), Nan Zhang(张楠), Xiaoyong Wei(魏晓勇)
Chin. Phys. B, 2018, 27 (**12**): 127702. DOI: 10.1088/1674-1056/27/12/127702

## Critical exponents of ferroelectric transitions in modulated $SrTiO_3$： Consequences of quantum fluctuations and quenched disorder

Wang Jing-Xue (王景雪), Liu Mei-Feng (刘美风), Yan Zhi-Bo (颜志波), Liu Jun-Ming (刘俊明)
Chin. Phys. B, 2013, 22 (**7**): 077701. DOI: 10.1088/1674-1056/22/7/077701

---

# Understanding thermal hysteresis of ferroelectric phase transitions in $BaTiO_3$ with combined first-principle-based approach and phase-field model

Cancan Shao(邵灿灿)[1,2,3] and Houbing Huang(黄厚兵)[1,2,3,†]

[1] *Beijing Institute of Technology, Zhuhai Beijing Institute of Technology, Zhuhai* 519088, *China*
[2] *School of Materials Science and Engineering, Beijing Institute of Technology, Beijing* 100081, *China*
[3] *Advanced Research Institute of Multidisciplinary Science, Beijing Institute of Technology, Beijing* 100081, *China*

(Received 16 August 2024; revised manuscript received 13 December 2024; accepted manuscript online 13 December 2024)

Based on the principles of thermodynamics, we elucidate the fundamental reasons behind the hysteresis of spontaneous polarization in ferroelectric materials during heating and cooling processes. By utilizing the effective Hamiltonian method in conjuction with the phase-field model, we have successfully reproduced the thermal hysteresis observed in ferroelectric materials during phase transitions. The computational results regarding the electrocaloric effect from these two different computational scales closely align with experimental measurements. Furthermore, we analyze how the first-order ferroelectric phase transition gradually diminishes with an increasing applied electric field, exhibiting characteristics of second-order-like phase transition. By employing the characteristic parameters of thermal hysteresis, we have established a pathway for calculations across different computational scales, thereby providing theoretical support for further investigations into the properties of ferroelectric materials through concurrent multiscale simulations.

**Keywords:** ferroelectric phase transition, thermal hysteresis, multiscale simulation, effective Hamiltonian, phase-field model

**PACS:** 77.22.Ej, 47.11.St, 77.80.B–

**DOI:** 10.1088/1674-1056/ad9e94 **CSTR:** 32038.14.CPB.ad9e94

## 1. Introduction

Multiscale modeling, a coupling method that integrates models across different scales, has become increasingly vital in addressing cross-length scale challenges in materials over the past few decades. The primary approach involves employing finer-scale computational models in the core part of the simulation system while utilizing coarse-scale simulation methods in the peripheral areas to capture the behavior of materials across continuous scales.[1–3] There are two main categories of material multiscale modeling strategies: the sequential multiscale methodology and the concurrent multiscale methodology.[4–6] The first strategy involves defining the effective properties of materials at lower scales and transferring them to higher-scale models, representing a stepwise process from small to large scales, or a parameter transfer process. However, this low-scale modeling methodology presents significant challenges, as it is weakly coupled across different scales. In contrast, the latter strategy simultaneously models and solves problems at various scales, offering the advantage of accurately reflecting the transfer behavior of effective properties at each scale. Consequently, it is both more efficient and more challenging than the sequential approach.

Since Valasek discovered the ferroelectric properties of Rochelle salt more than 100 years ago,[7] numerous theories have been proposed to explain the origin and mechanisms of ferroelectricity across different length scales. These theories include first-principles approaches at the nanoscale,[8] molecular dynamics modeling at the microscale, phase-field methods at the mesoscale, and macroscopic finite element analysis. In 1969, Lines examined ferroelectrics from both microscopic and macroscopic perspectives.[9] Over the years, research has explored the connection between first-principles and second-principle approaches,[10,11] progressively bridging parameters from the compositional level to the macroscopic collective level.[12] There have also been attempts to integrate the phase-field model into multiscale simulations of ferroelectrics.[13–17] The aforementioned multiscale calculation processes can be classified as sequential multiscale methods. However, such methods require effective parameter transfer between adjacent length scales, making it challenging to complete simulations that span from the nanoscopic to the macroscopic scale. In contrast, concurrent multiscale methods do not involve information transfer between fine and coarse scale; instead, both scales are solved simultaneously.[18,19] An equally important objective of multiscale models is the ability to map continuum-scale descriptions, such as deformation or temperature fields, onto smaller-scale features, such as the relative positions and velocities of atoms or grains.[3] Therefore, for homogeneous

†Corresponding author. E-mail: hbhuang@bit.edu.cn

© 2025 Chinese Physical Society and IOP Publishing Ltd. All rights, including for text and data mining, AI training, and similar technologies, are reserved.

materials, it is relatively straightforward to connect fine and coarse scales using the fundamental properties of the material.

In this study, we investigate the phenomenon of thermal hysteresis in ferroelectric materials during first-order and second-order phase transitions, utilizing Landau's theory of phase transition thermodynamics. Our research elucidates the underlying mechanisms of thermal hysteresis in these materials. We employ two theoretical models with distinct computational scales: the effective Hamiltonian method and the phase-field method. These models enable us to explore the phase transition behavior and electrocaloric effect of ferroelectric materials before and after the transition from the ferroelectric to the paraelectric phase at both micro and mesoscopic levels. Based on two different scale computational models, we demonstrate the characteristic property of thermal hysteresis in ferroelectric materials. This property can be measured at both the micro and meso levels by plotting the thermal hysteresis behavior associated with different phase transition types in ferroelectric materials, both with and without electric field effects. Additionally, we explore the relationship between electric field strength, spontaneous polarization, and thermal hysteresis. We establish the feasibility of a cross-length scale simulation bridge, transitioning from molecular dynamics based on first-principles at the micro level to phase-field modeling at the meso level. This approach provides a theoretical foundation for concurrent multiscale simulations and full chain design of ferroelectric materials in the future.

## 2. Methods

### 2.1. First-principle-based approach

The effective Hamiltonian approach to modeling ferroelectric perovskites was first proposed in the mid-1990s by Zhong, Rabe, and Vanderbilt.[20,21] This method utilizes an expansion of the total energy of the cubic perovskite crystal in terms of the soft mode responsible for the ferroelectric phase transition.[22,23] Both theoretical calculations and experimental results indicate that only small displacements in atomic positions from the perfect cubic structure lead to the ferroelectric phase in perovskites.[20] Consequently, the effective Hamiltonian is constructed as a Taylor series in displacements from the ideal cubic paraelectric structure[20]

$$\begin{aligned} E^{\mathrm{FE}}(\{u\},\{\eta\}) &= E^{\mathrm{self}}(\{u\}) + E^{\mathrm{dpl}}(\{u\}) \\ &\quad + E^{\mathrm{short}}(\{u\}) + E^{\mathrm{elas}}(\{\eta\}) \\ &\quad + E^{\mathrm{int}}(\{u\},\{\eta\}). \end{aligned} \tag{1}$$

The terms are the self-energy terms of isolated local modes. This energy contribution arises from a long-range dipole–dipole interaction, a short-range coupling between neighboring soft modes, the elastic energy, and the interaction between local modes and local strains, respectively. The specific expansion of each energy term is as follows:[20,24]

$$\begin{aligned} E^{\mathrm{self}} &= \sum_i E(u_i) = \sum_i \left[\kappa_2 u_i^2 + \alpha u_i^4 \right. \\ &\quad \left. + \gamma\left(u_{ix}^2 u_{iy}^2 + u_{iy}^2 u_{iz}^2 + u_{iz}^2 u_{ix}^2\right)\right], \end{aligned} \tag{2}$$

$$E^{\mathrm{dpl}}(\{u\}) = \frac{Z^{*2}}{\varepsilon_\infty} \sum_{i\neq j} \frac{u_i\cdot u_j - 3\left(\hat{R}_{ij}\cdot u_i\right)\left(\hat{R}_{ij}\cdot u_j\right)}{R_{ij}^3}, \tag{3}$$

$$E^{\mathrm{short}}(\{u\}) = \frac{1}{2}\sum_{i\neq j}\sum_{\alpha\beta} J_{ij,\alpha\beta} u_{i\alpha} u_{j\beta}, \tag{4}$$

$$\begin{aligned} E^{\mathrm{elas}}(\{\eta\}) &= \frac{N}{2} B_{11}\left(\eta_1^2 + \eta_2^2 + \eta_3^2\right) \\ &\quad + N B_{12}\left(\eta_1\eta_2 + \eta_2\eta_3 + \eta_1\eta_3\right) \\ &\quad + \frac{N}{2} B_{44}\left(\eta_4^2 + \eta_5^2 + \eta_6^2\right), \end{aligned} \tag{5}$$

$$E^{\mathrm{int}}(\{u\},\{\eta\}) = \frac{1}{2}\sum_i \sum_{l\alpha\beta} B_{l\alpha\beta}\eta_{i,l} u_{i,\alpha} u_{i,\beta}, \tag{6}$$

where parameters $\kappa_2$, $\alpha$, and $\gamma$ are determined by the first-principles calculations. The coefficients of other parameters can be obtained from Ref. [20]. The self-energy term is Taylor expansion based on the soft modes in each unit cell of ferroelectric materials, which conforms to the free energy expansion term of Landau theory of phase transition.

We use feram code to perform molecular dynamics simulations on the BTO[25] supercell $L_x \times L_y \times L_z = 16\times16\times16$ with an effective Hamiltonian, using a Nosé–Poincaré thermostat in a canonical ensemble. For the simulation without an electric field, we first thermalize the entire system with $2\times10^5$ time steps during heating and cooling, and then use $2\times10^5$ time steps for averaging the properties, with each time step set to 2 fs. For the simulation with an electric field applied, we use a larger temperature step, scanning from 320 K to 440 K in increments of 1 K/step. To simulate the thermal expansion process, we set an effective negative pressure term $p = -0.004T$ GPa related to temperature. During the heating and cooling processes, we set the initial configurations $\langle u_a\rangle = 0.11$ Å, $\langle u_a^2\rangle - \langle u_a\rangle^2 = (0.02\ \text{Å})^2$, and $\langle u_a\rangle = 0.0$ Å, $\langle u_a^2\rangle - \langle u_a\rangle^2 = (0.03\ \text{Å})^2$, respectively.

### 2.2. Phase-field model

The thermodynamically motivated phase-field method can provide the phase transition process of a material, which considers the phase transition process of a material as an evolution equation of a physical field in the material, which can be temperature, chemical components, phase composition, *etc*. By modeling the evolution equation of the physical field, the phase-field simulation can simulate the material's microscopic results and macroscopic properties in the phase transformation process. The ferroelectric phase-field equations use the spontaneous polarization $P$ as the order parameter, and

the microstructure evolution is realized by solving the time-dependent Ginzburg–Landau equation[26–30]

$$\frac{\partial P_i(\boldsymbol{r},t)}{\partial t} = -L\frac{\delta F}{\delta P_i(\boldsymbol{r},t)}, \quad i = x,y,z, \tag{7}$$

where $r$, $t$, and $P_i(\boldsymbol{r},t)$ represent space vector position, time, and polarization components, respectively. $L$ is the kinetic coefficient, and $F$ is the total free energy of the system, including the bulk free energy (i.e., Landau energy), the elastic energy, the electrostatic field energy, and the gradient energy (i.e., domain wall energy), has the following expression:

$$\begin{aligned} F &= F_{\text{Land}} + F_{\text{elas}} + F_{\text{elec}} + F_{\text{grad}} \\ &= \iiint_V (f_{\text{Land}} + f_{\text{grad}} + f_{\text{elas}} + f_{\text{elec}})\,\mathrm{d}V, \end{aligned} \tag{8}$$

$$f_{\text{Land}} = \alpha_i P_i^2 + \alpha_{ij} P_i^2 P_j^2 + \alpha_{ijk} P_i^2 P_j^2 P_k^2, \tag{9}$$

$$f_{\text{grad}} = \frac{1}{2} g_{ijkl} P_{i,j} P_{k,l}, \tag{10}$$

$$f_{\text{elas}} = \frac{1}{2} c_{ijkl} e_{ij} e_{kl} = \frac{1}{2} c_{ijkl} \left(\varepsilon_{ij} - \varepsilon_{ij}^0\right)\left(\varepsilon_{kl} - \varepsilon_{kl}^0\right), \tag{11}$$

$$f_{\text{elec}} = -P_i(r) E_i(r) - \frac{1}{2}\varepsilon_0 \kappa_{ij}^b(r) E_i(r) E_j(r), \tag{12}$$

where $\alpha_i$, $\alpha_{ij}$, and $\alpha_{ijk}$ are the Landau coefficients corresponding to the expansion of polarization $P$ to the sixth order, $P_{i,j} = \partial P_i/\partial x_j$, $g_{ijkl}$ is the gradient coefficient of the polarization distribution in space.[29] The relevant parameters of the phase-field method for BTO can be found in relevant literature.[31–33]

The above phase-field equation is solved using the semi-implicit Fourier transform spectral method. The simulated BTO size is $16\Delta x \times 16\Delta y \times 16\Delta z$, where $\Delta x = \Delta y = \Delta z = 1$ nm. The mechanical and electrical boundary conditions of the bulk case are used, and the calculation is based on the random domain structure as the initial state for evolution. Under the condition of not applying an electric field, we set a $2 \times 10^4$ time step evolution for every 1-K increase or decrease for the heating and cooling processes, and increase thermal fluctuation so that BTO can cross potential barriers.

## 3. Results and discussion

To better understand the phenomenon of thermal hysteresis in ferroelectrics during the heating and cooling processes associated with phase transitions, we analyze the temperature dependence of the free energy curve of ferroelectric spontaneous polarization. When the temperature is exceeds $T_2$, the Gibbs free energy ($G$) exhibits a local minimum only at $P = 0$, indicating that the system is in the paraelectric phase, characterized by the absence of spontaneous polarization. Conversely, when $T$ is less than $T_0$, $G$ presents two minima corresponding to $-P$ and $+P$, signifying that the system is in the ferroelectric phase, which allows for two possible states of spontaneous polarization with equal and opposite signs. $G$ exhibits a third minimum at $P = 0$ at temperatures slightly above $T_C$. This value is greater than the other two minima, indicating that the paraelectric phase can exist as a metastable state. At $T = T_C$, the three minima are equal, meaning that the paraelectric and ferroelectric phases are energetically equally favorable. When $T$ is slightly above $T_C$, the minimum at $P = 0$ is lower than the other two minima, suggesting that the paraelectric phase is stable while the ferroelectric phase is metastable. As the temperature increases slightly beyond $T_1$, the minima on both sides vanish, but two inflection points remain on the curve. The disappearance of the minima indicates that the ferroelectric phase cannot exist, even as a metastable state. The presence of two inflection points implies that the application of an electric field can induce the ferroelectric phase. However, when the temperature rises further above $T_2$, the inflection points disappear, and the electric field can no longer induce a ferroelectric phase. Notably, when cooling through the $T_C$ point, the material retains its metastable paraelectric phase even above $T_C$. Conversely, while heating through the $T_C$ point, the material maintains its metastable ferroelectric phase, indicating that the $T_C$ measured during cooling is lower than that measured during heating. As illustrated in Fig. 1(b), the spontaneous polarization of the ferroelectric material varies with temperature and follows different trajectories during heating and cooling. This discrepancy is the fundamental cause of thermal hysteresis in ferroelectric materials during these processes.

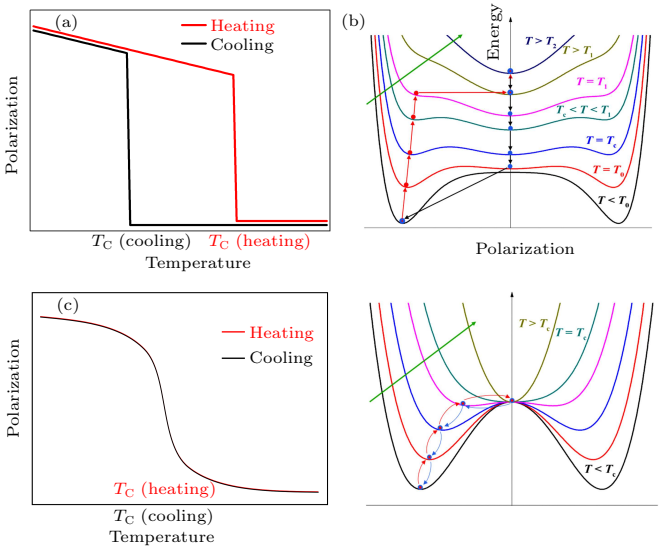



**Fig. 1.** Schematic diagram of the temperature dependence of the ferroelectric spontaneous polarization in case of (a) a first-order and (c) a second-order phase transition. Free energy as a function of polarization at various temperatures in case (b) a first-order and (d) a second-order phase transition. The light green arrow indicates the direction of the temperature increase.

When a ferroelectric material is in the ferroelectric phase and is heated, the curve representing the $P$ of the material as a function of temperature is depicted by the red solid line in the figure. As the material approaches the $T_C$ during heating,

it transitions to the paraelectric phase. When the ferroelectric material cools from a high temperature to a low temperature within the paraelectric phase, the curve illustrating the change in the magnitude of the polarization with temperature follows the path of the black solid line, allowing the material to remain in the ferroelectric phase at temperatures below $T_C$. The material transitions to the paraelectric phase once the phase transition temperature is reached. If the material is subsequently heated again, it will follow the red solid path, and this process continues. The two $P$–$T$ curves coincide at either the fully paraelectric or ferroelectric phase. The discontinuity observed in these curves represents the latent heat generated by the first-order phase transition in a ferroelectric material.[34,35]

However, there is no concept of thermal hysteresis for ferroelectrics exhibiting second-order phase transitions. As illustrated in Figs. 1(c) and 1(d), the curve of $G$ *versus* temperature for a second-order ferroelectric material shows that the minimum point of $P$ follows the same trajectory during both heating and cooling processes. In the polarization versus temperature curve, the phase transition temperature during heating does not equal that during cooling, as depicted in Fig. 1(b). This discrepancy is referred to as thermal hysteresis. The presence or absence of thermal hysteresis serves as a crucial indicator for distinguishing between first-order and second-order phase transitions in ferroelectric materials, and it is also a key parameter for experimentally determining the type of phase transition. Investigations into thermal hysteresis have been conducted across various scales of ferroelectric material simulations.[1,12,36,37] The earliest theoretical efforts concentrated on macroscopic models grounded in solid thermodynamic theory to describe the macroscopic behavior of ferroelectrics.[38] These studies primarily considered three different scales: domains, grains, and polycrystals.[39–41] However, there is a notable lack of descriptions extending from the microscopic to the mesoscopic level. Therefore, it is essential to explore the phenomenon of thermal hysteresis in ferroelectric materials from the microscale to the mesoscale.

In this article, we employ two distinct methods for calculating length scales: the effective Hamiltonian method and the phase-field method, to investigate the thermal hysteresis phenomenon associated with first-order phase transitions in ferroelectric materials. Our analysis of these two calculation models leads us to conclude that the effective Hamiltonian method is grounded in the development of the soft mode model, while the phase-field method utilizes $P$ as the order parameter, both of which are rooted in thermodynamic phase transition theory. Both methods can effectively represent the potential energy relationships within ferroelectric systems. Consequently, we will consider thermal hysteresis as an effective property that facilitates the transition from microscopic to mesoscopic calculations, thereby enabling the development of concurrent multiscale analyses of ferroelectric phase transitions. Importantly, the expressions derived from the two different scale models indicate that the effective Hamiltonian method is based on the soft mode theory, which formulates the energy terms of the system. The phase transition of the system arises from the combined effects of the lattice structure within the crystal, with the unit cell serving as the fundamental component of the effective Hamiltonian method. In this study, we employed a lattice size of $L_x \times L_y \times L_z = 16 \times 16 \times 16$ in the effective Hamiltonian method, corresponding to the dimensions of the unit cell. For the phase-field method, we utilized samples at a $16 \times 16 \times 16$ nanometer scale for our research. The phase-field method divides the spatial grid, resulting in a calculated spatial scale that is significantly larger than that of the unit cell. If the scale of the effective Hamiltonian is expanded to the mesoscopic scale, or if the spatial grid of the phase-field method is subdivided more densely to the angstrom scale, the computational cost becomes a primary consideration.

In this study, we focus on the classic $ABO_3$ perovskite material, barium titanate ($BaTiO_3$, BTO), as our research subject. At the nanoscale, we employ the effective Hamiltonian method to calculate the heating and cooling processes of BTO. The specific calculation parameters are detailed in the theoretical methods section.[42] In the heating calculation for BTO, we initially set the polarization displacement of the soft mode configuration to 0.11 Å, causing the ions in the system to deviate from their equilibrium positions and maintain a ferroelectric state. During the cooling process, we adjust the polarization displacement of the soft mode configuration to 0 Å, allowing the ions to return to their equilibrium positions and achieve a paraelectric state. From Fig. 2(a), we can observe the $P$–$T$ relationship curve derived from the heating and cooling processes. The red solid line represents the heating process, while the black solid line indicates the cooling process. The $T_C$ for the heating curve of the ferroelectric material is 403 K, whereas the $T_C$ for the cooling curve is 362 K. The $T_C$ obtained from the ferroelectric heating curve is higher than that from the cooling curve, with a difference of 41 K. This indicates that during the heating process, the $T_C$ of ferroelectric material is greater than during the cooling process. This observation further confirms the inconsistency in the $P$–$T$ curves observed during the heating and cooling phases of the ferroelectric first-order phase transition.

In the mesoscale aspect, we employ the phase-field model to analyze the heating and cooling processes of BTO. We utilize the low-temperature ferroelectric domain as the initial domain structure during heating and the high-temperature paraelectric phase as the initial evolution structure during the cooling. The resulting $P$–$T$ curve is illustrated in Fig. 3(b). During

the heating process, the $T_C$ obtained from the heating curve (solid red line in Fig. 3(b)) is 402 K, while the Curie transition temperature derived from the cooling curve is 373 K. Notably, the $T_C$ from the heating curve exceeds that of the cooling curve by 29 K, which aligns with the findings from previous microscale calculations. By comparing the experimental results of the transition temperatures from the BTO heating and cooling curves, we demonstrate that the results obtained through our effective Hamiltonian method and the phase-field method not only replicate the phenomenon of positive thermal hysteresis but also corroborate the findings from these two distinct calculation scales with the experimental data. This consistency provides strong evidence for the reliability of the two different scale calculation models we have selected.

To better understand the structural diagrams of the two calculation methods before and after the phase transition during the heating and cooling processes of BTO, we selected four light blue solid dots in Fig. 2(a), labeled I, II, III, and IV. Points I and II represent the pre- and post-ferroelectric transitions that occur during the heating of BTO using the feram code,[43,44] while points III and IV represent the pre- and post-ferroelectric transitions during cooling. The four types of dipole configurations depicted in Fig. 2(b) correspond to the four points observed before and after the heating/cooling process illustrated in Fig. 2(a). As the system we are examining is a three-dimensional system, to comprehend the specific distribution of the dipole configuration in a certain direction, we chose to study the dipole configuration along the $yOz$ plane at the intersection of $x = 8$ to analyze the dipole distribution before and after the phase transition. The dipole arrangement prior to the ferroelectric phase transition is more ordered than the distribution observed after the phase transition, indicating the material's transition from the ferroelectric phase to the paraelectric phase. Additionally, figure 2(b) illustrates the dipole distribution along the $+z$ and $-z$ directions before and after the ferroelectric phase transitions, where the red hollow symbols represent upward dipoles and blue solid symbols represent downward dipoles. This also reflects the transition of the dipoles from an ordered to a disordered state. To calculate the heating curve of the BTO using the phase-field method, we also captured the polarization distribution diagram of the system at its midpoints.

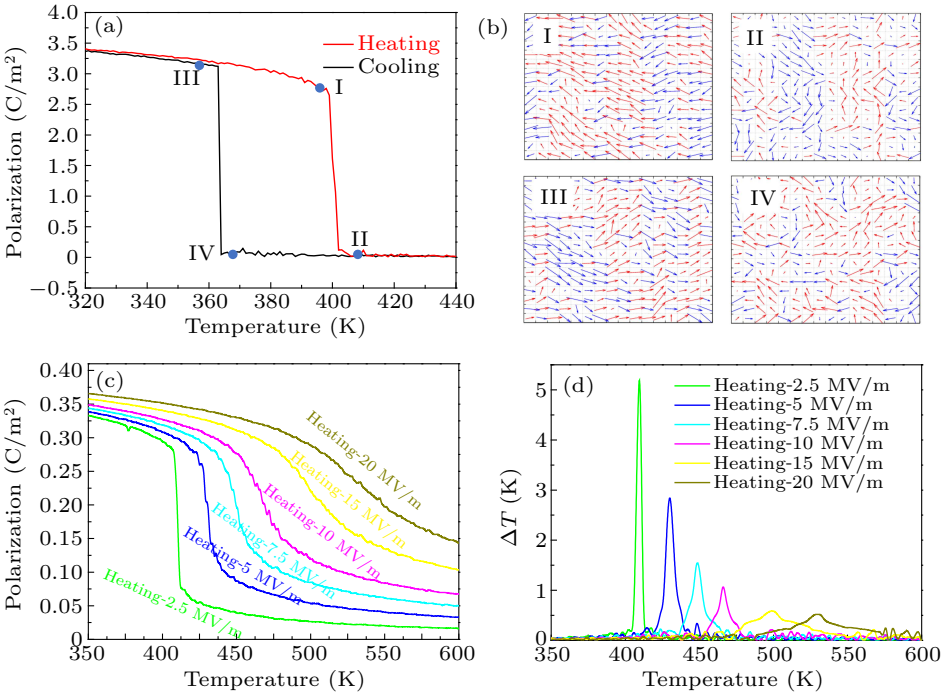



**Fig. 2.** The effective Hamiltonian method calculated the *P*–*T* curve of the first-order ferroelectric material during the heating and cooling processes. Panel (b) is the distribution of local modes in the cell at different temperatures, where I, II, III, and IV correspond to the points on the curve in panel (a). (c) The *P*–*T* curve under different electric fields is applied during the heating process. (d) The relationship between adiabatic temperature change and temperature is calculated in panel (c).

Similarly, by analyzing points I–IV in Fig. 3(b), we can draw the same conclusion regarding the scale of the phase-field calculation. The polarization at point III in Fig. 3(b) is greater than that at point I, which aligns with the observation that ferroelectric polarization decreases as temperature increases. Since the phase-field method utilizes a larger grid scale, the polarization distribution map of the system, which represents the ferroelectric domain, remains a single domain prior to the ferroelectric transition. However, after the ferroelectric transition, the polarization distribution becomes disordered, and the concept of domainlessness characterizes the paraelectric phase.

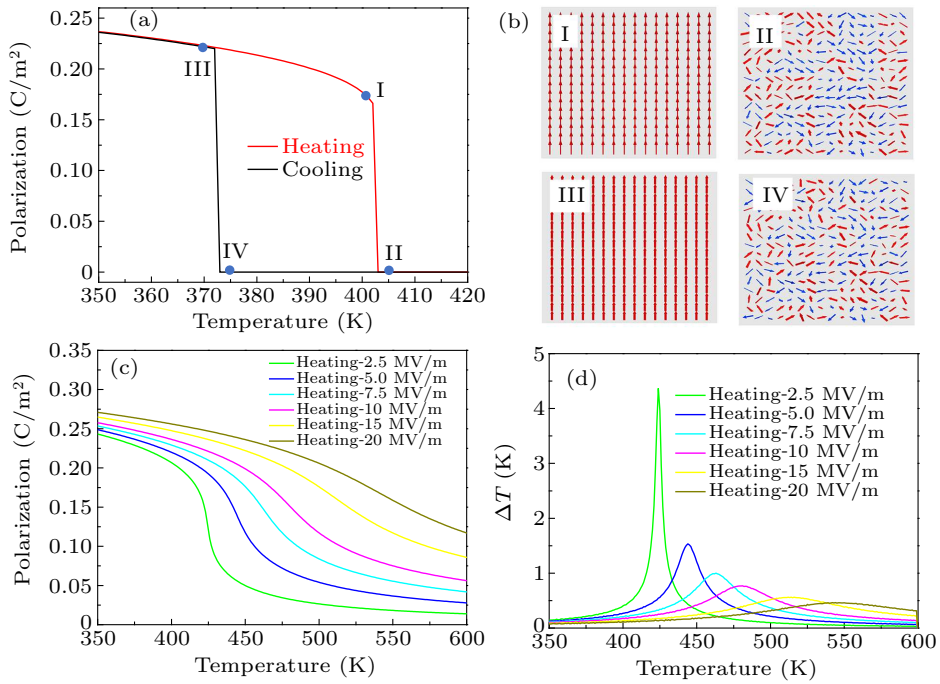



**Fig. 3.** The phase-field method calculated the *P*–*T* curve of the first-order of ferroelectric material during the heating and cooling processes. Panel (b) is the distribution of polarization in unit grid at different temperatures, where I, II, III, and IV correspond to the points on the curve in panel (a). (c) The *P*–*T* curve under different electric fields is applied during the heating process. (d) The relationship between adiabatic temperature change and temperature is calculated in panel (c).

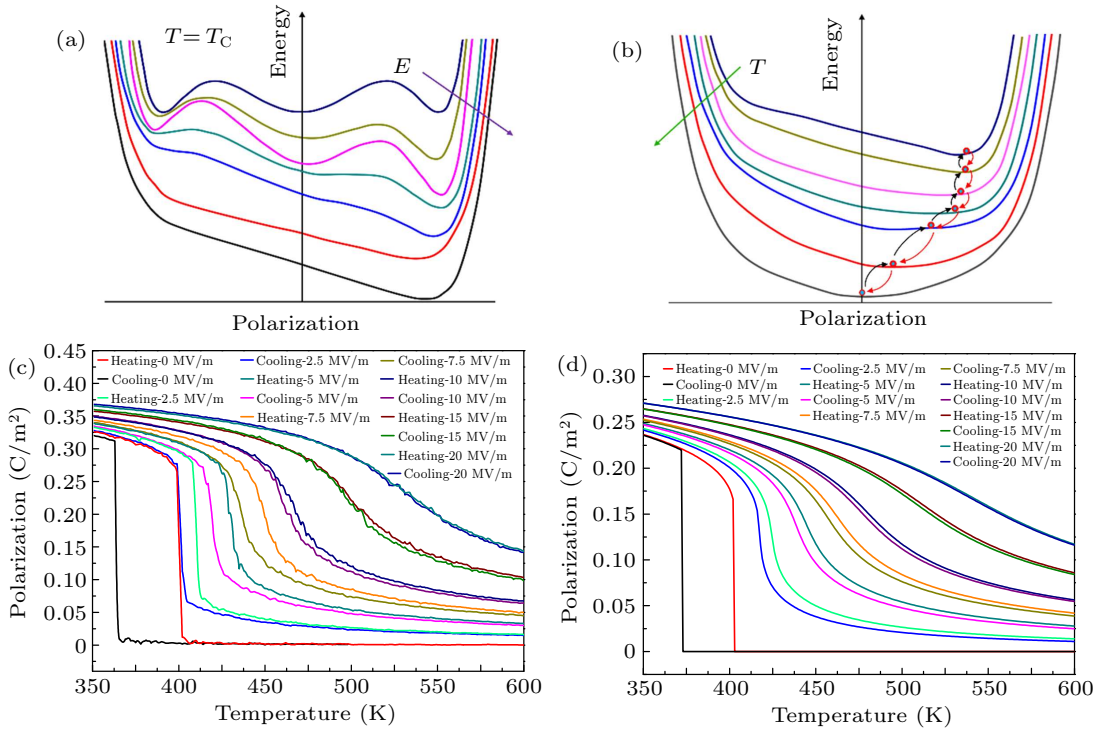



**Fig. 4.** (a) Schematic diagram of the Gibbs free energy curve of the first-order phase transitions of ferroelectric material at $T_C$ as the applied electric field gradually increases. (b) Schematic diagram of the Gibbs free energy curve of ferroelectric spontaneous polarization with temperature when the constant electric field remains unchanged. Panels (c) and (d) are the heating/cooling curves of ferroelectric as a function of temperature under different electric field strengths in the effective Hamiltonian and phase-field methods, respectively.

Based on the Maxwell relation $(\partial P/\partial T)_E = (\partial S/\partial E)_T$, the adiabatic temperature change ($\Delta T$) can be calculated as follows:

$$\Delta T = -T \int_{E1}^{E2} \frac{1}{C_{P,E}} \left( \frac{\partial P}{\partial T} \right) \mathrm{d}E.$$

The applied electric field varies from $E_1$ to $E_2$ ($\Delta E = E_2 - E_1$), and $C_{P,E}$ represents the specific heat at constant pressure and applied electric field. The specific heat value, $C_E = 3.25 \times 10^6$ J·K$^{-1}$·m$^{-3}$, corresponds to measurements taken at room temperature. As illustrated in Figs. 2(d) and 3(d), both calculation models yield similar results: $P$ increases gradually with

the strength of the electric field, and $\Delta T$ also rises with increasing electric field strength. When the electric field strength reaches 2 MV·m$^{-1}$, $\Delta T$ approaches nearly 4 K.

When a ferroelectric material undergoes a first-order phase transition at $T_C$, the minimum value of the $G$ curve for the material shifts in the direction of the applied electric field. As the strength of the applied electric field increases, this shift becomes more pronounced, as shown in Fig. 4(a). Figures 4(c) and 4(d) demonstrate that as the electric field gradually intensifies, the downward trend of the $P$–$T$ curve is progressively diminished during the ferroelectric first-order phase transition. As the temperature increases, the minimum value of the $G$ for the ferroelectric material shifts to the left when a constant electric field is applied, as shown in Fig. 4(b). Conversely, it shifts to the right under conditions of decreasing electric field strength. This process follows the same evolutionary path as the minimum values observed in the heating and cooling curves of second-order ferroelectrics, indicating the absence of thermal hysteresis. Furthermore, figures 4(c) and 4(d) reveal that as the electric field strength increases, the thermal hysteresis phenomenon between the heating and cooling curves of the ferroelectric first-order phase transition gradually diminishes until it ultimately disappears.

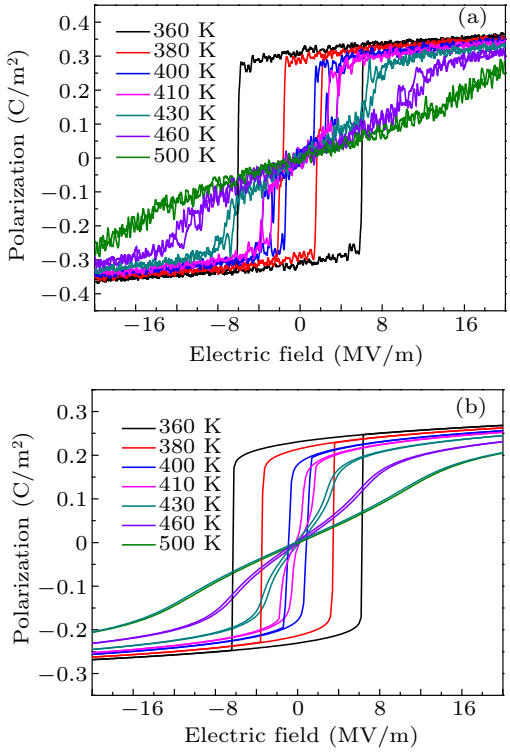



**Fig. 5.** The ferroelectric polarization ($P$)–electric field ($E$) hysteresis loop ($P$–$E$ loop) of (a) the effective Hamiltonian method and (b) the phase-field method at different temperatures.

Based on the analysis presented above, we can conclude that when the electric field is sufficiently strong, a first-order ferroelectric can undergo a transformation into a second-order phase transition. We also examined the relationship between ferroelectric polarization and electric field strength ($P$–$E$ loop) for two length-scale models at various temperatures, as illustrated in Fig. 5. Both scale calculation models confirm that as the temperature increases, the shape of the $P$–$E$ loop transitions from wide to narrow, while the coercive field gradually decreases. No polarization *versus* electric field loops was observed above 500 K.[45]

## 4. Conclusion

BTO, a classic ferroelectric material that exhibits a first-order phase transition, demonstrates thermal hysteresis during both heating and cooling: an intrinsic characteristic of ferroelectric first-order phase transitions. The effective Hamiltonian method, developed as a soft mode theory, along with the phase-field method, which is based on order parameters, are computational models derived from Landau's phase transition theory. Both simulation approaches can accurately reproduce the ferroelectric first-order phase transition and generate thermal hysteresis. We have developed a concurrent multiscale computational model to study the first-order phase transition of ferroelectric materials, which a particular focuse on thermal hysteresis as an effective property. The $P$–$T$ curves are utilized to analyze the correlation properties of ferroelectrics. In this study, we examine the electrocaloric effect on the $P$–$T$ curves under varying electric field strengths at two distinct calculation scales. Our results demonstrate a consistent electrocaloric temperature change derived from the models at both length scales. This work aims to facilitate the construction and investigation of concurrent multiscale computational models for ferroelectric materials by bridging the gap between atomiclevel and macroscopic continuum behavior through the lens of thermal hysteresis.

## Acknowledgements

Project supported financially by the National Natural Science Foundation of China (Grant No. 52372100) and the National Key Research and Development Program of China (Grant No. 2019YFA0307900).

## References

[1] Tino G, Adrià G C, Maximilian F, Andreas T, Lukas P, Lluís M, Antoni P, Konstantin P S and Gutfleisch O 2018 *Nat. Mater.* **17** 929
[2] Lee J D, Li J, Zhang Z and Wang L 2018 *Sequential and Concurrent Multiscale Modeling of Multiphysics: From Atoms to Continuum* In *Micromechanics and Nanomechanics of Composite Solids* (Ed. by Meguid S and Weng G) (Cham: Springer)
[3] Fish J, Wagner G J and Keten S 2021 *Nat. Mater.* **20** 774
[4] John G M, Farhat C and Fish J 2005 *J. Comput. Inf. Sci. Eng.* **5** 198
[5] Lu G, Tadmor E B and Kaxiras E 2006 *Phys. Rev. B.* **73** 024108
[6] Wing K, Liu S, Hao J, *et al.* 2003 *Multiscale analysis and design in heterogeneous system* In *Proceeding of VII International Conference on Computational Plasticity, Barcelona* (Ed. by Onate E and Owen D R J)
[7] Valasek J 1921 *Phys. Rev.* **17** 475
[8] Ghosez P and Junquera J 2022 *Annu. Rev. Condens. Matter Phys.* **13** 325
[9] Lines M E 1969 *Phys. Rev.* **177** 797

[10] Sato M, Kumada A, Hidaka K, Yasuoka T, Hoshina Y and Shiiki M 2023 *IEEE Tran. Dielecr. Electr. Insul.* **30** 674
[11] Lu G, Tadmor E B and Kaxiras E 2006 *Phys. Rev. B.* **73** 024108
[12] Huang J, Zhuang Q, Hu Y, Yu Q and Liu S 2022 *Ferroelectrics Advances in fundamental studies and emerging applications* (IOP Publishing Ltd) pp. 3–22
[13] Wakili R, Lange S and Ricoeur A 2023 *Comput. Mech.* **72** 1295
[14] Pešiü M, Lecce VD, Pramanik D and Larcher L 2018 *International Conference on Simulation of Semiconductor Processes and Devices*, 2018, Austin, USA, pp. 111–114
[15] Völker B, Lanis C M and Kamlah M 2012 *Smart Mater. Struct.* **21** 035025
[16] Völker B, Marton P, Elsässer C and Kamlah M 2011 *Continuum Mech. Thermodyn.* **23** 435
[17] Wang J, Wang B and Chen L 2019 *Ann. Rev. Matter. Res.* **49** 127
[18] He C, Ge J, Qi D, Gao J, Chen Y, Liang J and Fang D N 2019 *Compos. Sci. Technol.* **171** 21
[19] Liu B, Kovachki N, Li Z, Azizzadenesheli K, Anandkumar A, Stuart A M and Bhattacharya K 2022 *J. Mech. Phys.* **158** 104668
[20] Zhong W, Vanderbilt D and Rabe K M 1995 *Phys. Rev. B.* **52** 6301
[21] Zhong W, Vanderbilt D and Rabe K M 1994 *Phys. Rev. Lett.* **73** 1861
[22] Campbell D S 1976 *Phys. Bull.* **27** 124
[23] King-Smith R D and Vanderbilt D 1994 *Phys. Rev. B* **49** 1651
[24] Beckman S P, Wan L F, Barr H A and Nishimatsu T 2012 *Mater. Lett.* **89** 254
[25] Yang Y, Bellaiche L and Xiang H 2022 *Chin. Phys. Lett.* **39** 097701
[26] Devonshire A F 1949 *XCVI. Theory of barium titanate - Part I*, Series 7, (Taylor & Francis Online) pp. 1040–1063
[27] Devonshire A F 1949 *CIX. Theory of barium titanate - Part II*, Series 7, (Taylor & Francis Online) pp. 1040–1063
[28] Devonshire A F 1954 *Adv. Phys.* **3** 85
[29] Chen L 2002 *Ann. Rev. Mater. Res.* **32** 113
[30] Guo C and Huang H 2022 *Microstructures* **2** 2022021
[31] Wang J, Wu P, Ma X and Chen L 2010 *J. Appl. Phys.* **108** 114105
[32] Huang Y, Wang J, Yang T, Wu Y, Ma X and Chen L 2018 *Appl. Phys. Lett.* **112** 102901
[33] Qin H, Zhao J, Chen X, Li H, Wang S, Du Y, Zhou H, Li P and Wang D 2023 *Microstructures* **3** 2023035
[34] Liu Y, Aziguli H, Zhang B, Xu W, Lu W, Bernholc J and Wang Q 2018 *Nature* **562** 96
[35] Wei X, Prokhorenko S, Wang B, Liu Z, Xie Y, Nahas Y, Jia C, Dunin-Borkowski R E, Mayer J, Belleiche L and Ye Z 2021 *Nat. Commun.* **12** 5322
[36] Li Z, Wu H, Li J, Wang S, Qin S, He J, Liu C, Su Y, Qiao L, Lookman T and Bai Y 2022 *Acta Mater.* **228** 117784
[37] Liu Y, Haibibu A, Xu W, Han Z and Wang Q 2020 *Adv. Funct. Mater.* **30** 2000648
[38] Li Z, Mao Z and Corcolla R 2023 *Mech. Mater.* **187** 104842
[39] Bassiouny E and Maugin G A 1989 *Int. J. Eng. Sci.* **27** 975
[40] Huber J, Fleck N, Landis C M and McMeeking R M 1999 *J. Mech. Phys. Solids* **47** 1663
[41] Mehling V, Tsakmakis C and Gross D 2007 *J. Mech. Phys. Solids* **55** 2106
[42] Tarnaoui M, Zaim M, Kerouad M and Zaim A 2019 *Phys. Lett. A* **384** 126093
[43] Nishimatsu T, Waghmare U V, Kawazoe Y and Vanderbilt D 2008 *Phys. Rev. B* **78** 104104
[44] Paul J, Nishimatsu T, Kawazoe Y and Waghmare U V 2007 *Phys. Rev. Lett.* **99** 077601
[45] Zhao J, Gao J, Li W, *et al.* 2021 *Nat. Commun.* **12** 747